



MOX–Report No. 21/2014

The benefits of anisotropic mesh adaptation for brittle fractures under plane-strain conditions

ARTINA, M.; FORNASIER, M.; MICHELETTI, S.; PEROTTO, S.

MOX, Dipartimento di Matematica “F. Brioschi”
Politecnico di Milano, Via Bonardi 9 - 20133 Milano (Italy)

mox@mate.polimi.it

<http://mox.polimi.it>

The benefits of anisotropic mesh adaptation for brittle fractures under plane-strain conditions

Marco Artina[†] Massimo Fornasier[†] Stefano Micheletti[#]
Simona Perotto[#]

May 26, 2014

[#] MOX– Modellistica e Calcolo Scientifico, Dipartimento di Matematica “F. Brioschi”
Politecnico di Milano, Piazza L. da Vinci 32, 20133 Milano, Italy
{stefano.micheletti,simona.perotto}@polimi.it

[†] Faculty of Mathematics, Technische Universität München
Boltzmannstrasse 3, 85748, Garching, Germany,
{marco.artina,massimo.fornasier}@ma.tum.de

Keywords: non-convex minimization, brittle materials, a posteriori error estimators, anisotropic mesh adaptation

AMS Subject Classification: 65N30, 65N50, 74R10, 74G65, 65K10

Abstract

We develop a reliable *a posteriori* anisotropic first order estimator for the numerical simulation of the Francfort and Marigo model of brittle fracture, after its approximation by means of the Ambrosio-Tortorelli variational model. We show that an adaptive algorithm based on this estimator reproduces all the previously obtained well-known benchmarks on fracture development with particular attention to the fracture directionality. Additionally, we explain why our method, based on an extremely careful tuning of the anisotropic adaptation, has the potential of outperforming significantly in terms of numerical complexity the ones used to achieve similar degrees of accuracy in previous studies.

1 Introduction

A variational formulation for the evolution of the fracture surface in a brittle, linearly elastic solid was proposed by Francfort and Marigo in [19]. The main feature of this model is that there is no predefined crack, i.e., the crack is able to propagate in the material without any constraint, driven only by elastic forces. Bourdin et al. [7] addressed the numerical approximation of the solution of the fracture model by Francfort and Marigo by first approximating it via the Ambrosio-Tortorelli variational model. Then, an extremely fine discretization is considered to be able to capture the fracture path and its expected directional developments, independently of the intrinsic anisotropies of the a priori prescribed mesh. This technique proved to be very stable not only in the case of anti-plane shear, but also in the more challenging situation where plane-strain is considered, capturing the physically expected crack paths and directionalities. However, the cost of an extremely fine discretization to render the material numerically homogenous is enormous, leading to the quest for possible alternative techniques based on adaptive strategies, which can break the ambiguity of *"the crack following the mesh or the mesh following the crack"*. In the work of Chambolle et al. [10], an anisotropic adaptive finite element method was presented for the simulation of the model of Francfort and Marigo in the anti-plane shear case. The adaptive re-meshing is, however, based on a local approximation of the Hessian of the solution, which, unfortunately, may lack the expected regularity. In the approach of Süli et al. [8], the adaptivity is driven exclusively by an *a posteriori* first order estimator, but only isotropic mesh refinement was considered. In our recent work [4], we tried to combine these two previous approaches, designing an appropriate *a posteriori* anisotropic first order estimator, leading to mesh coarsening far from the fracture and fine mesh elements exclusively very close to the crack path. Again this new method resulted being very efficient and effective, producing stable and realistic results for some test cases where the force applied to the domain is orthogonal to the domain itself. In this work, we study and present numerical results in the case the fracture is induced by a plane-strain. These tests play a key role in validating the reliability and the applicability of anisotropic mesh adaptation in the context of quasi-static crack path detection. Indeed, for assessing the quality of our results we can count on previous precise studies of the behaviour of the fracture, both from numerical and physical viewpoints [2, 7].

The numerical experiments in Sect. 4 show that the proposed method is very stable and it allows us to reproduce all the previously obtained predictions on fracture development, in particular its directionality features. Additionally, we expect that our method, based on an extremely careful tuning of the anisotropic adaptation, outperforms significantly the ones used to achieve similar degrees of accuracy in previous studies. Unfortunately, the only reference with which we can compare the computational burden is Süli et al. [8], while for Bourdin et al., Chambolle et al., Del Piero et al. [7, 10, 16] we are obliged to extrapolate

our positive expectation from the very fine meshes showed in the corresponding numerical sections.

The paper is organized as follows. In Sect. 1.1, we describe the model, in Sect. 2, we introduce the discrete setting and the anisotropic error estimator which drives the mesh adaptation. In Sect. 3, we provide the algorithm for the minimization of the energy functional, while in Sect. 4, we address the numerical results on the benchmark tests, comparing them with the expected ones from the literature.

1.1 The Mathematical Model of Plane-Strain Fracture

The considered model extends the anti-plane case proposed in [1] and, following [7], we introduce an isotropic linearly elastic constitutive law, i.e., the Plane-strain Ambrosio-Tortorelli functional

$$J^{PAT}(\mathbf{u}, v) = \frac{1}{2} \int_{\Omega} (v^2 + \eta) \boldsymbol{\sigma}(\mathbf{u}) : E(\mathbf{u}) \, d\mathbf{x} + \frac{1}{2} \int_{\Omega} [\alpha(1-v)^2 + \varepsilon |\nabla v|^2] \, d\mathbf{x}, \quad (1)$$

where $\Omega \subset \mathbb{R}^2$, the fields $\mathbf{u} : \Omega \rightarrow \mathbb{R}^2$ and $v : \Omega \rightarrow [0, 1]$ are the displacement and a smoothed crack path indicator, $0 < \eta \ll \varepsilon \ll 1$ and $\alpha = 1/(4\varepsilon)$ are suitable regularizing constants, $\boldsymbol{\sigma}(\mathbf{u}) = \lambda \operatorname{tr}(E(\mathbf{u})) I + 2\mu E(\mathbf{u})$, is the Cauchy stress tensor, with λ and μ the Lamé constants, and, where, for every $\mathbf{d} : \Omega \rightarrow \mathbb{R}^2$,

$$E(\mathbf{d}) = \begin{bmatrix} \frac{\partial d_1}{\partial x_1} & \frac{1}{2} \left(\frac{\partial d_1}{\partial x_2} + \frac{\partial d_2}{\partial x_1} \right) \\ \frac{1}{2} \left(\frac{\partial d_1}{\partial x_2} + \frac{\partial d_2}{\partial x_1} \right) & \frac{\partial d_2}{\partial x_2} \end{bmatrix}$$

is the symmetric gradient tensor, $T_1 : T_2$ denoting the tensor product between $T_1, T_2 : \Omega \rightarrow \mathbb{R}^{2 \times 2}$, and $\mathbf{x} = (x_1, x_2)^T \in \Omega$. In practice, v , with $0 \leq v \leq 1$, can be considered as a phase field for the crack interface [6, 28]. The first integral in (1) represents the elastic energy of the material, while the second integral models the energy associated with the crack propagation inside the material. The case $v = 1$ is the crack-free configuration, since the last integral vanishes. On the contrary, the regions where $v = 0$ identify the cracked area.

Let $0 = t_0 < \dots < t_F = T$ be a partition of the time window $[0, T]$. Let $\mathbf{g} : \Omega \times [0, T] \rightarrow \mathbb{R}^2$ be an displacement assigned over a subset $\Omega_D \subset \Omega$ which drives the fracture onset, i.e.,

$$\mathbf{g}(\mathbf{x}, t) = \begin{cases} \mathbf{g}_D(t) & \text{if } \mathbf{x} \in \Omega_D, \\ \mathbf{0} & \text{elsewhere.} \end{cases}$$

Notice that, with a view to the numerical test cases, function \mathbf{g}_D is assumed to be constant in space. We denote by $\mathcal{A}_k(\mathbf{g}) = \{\mathbf{u} \in [H^1(\Omega)]^2 : \mathbf{u}(\mathbf{x}) = \mathbf{g}(\mathbf{x}, t_k) \, \forall \mathbf{x} \in \Omega_D\}$ the space of the admissible solutions, i.e., the fields which coincide with \mathbf{g} on Ω_D at $t = t_k$. According to a quasi-static approximation [19],

the minimization of the functional J in (1) at the time level t_k consists of finding the pair $(\mathbf{u}(t_k), v(t_k))$, with $k = 0, \dots, F$, such that

$$\begin{aligned} (\mathbf{u}(t_k), v(t_k)) \in & \underset{\substack{\mathbf{u} \in \mathcal{A}_k(\mathbf{g}) \\ v \in H^1(\Omega; [0, 1]), v|_{CR_{k-1}} = 0}}{\operatorname{argmin}} J(\mathbf{u}, v), \end{aligned} \quad (2)$$

where $CR_{k-1} = \{\mathbf{x} \in \bar{\Omega} : v(t_{k-1}) < \text{CRTOL}\}$, with CRTOL a tolerance used to enforce the irreversibility of the crack. For simplicity we denote hereafter $\mathbf{g}(\mathbf{x}, t)$ with $\mathbf{g}(t)$. Moreover, standard notation is understood to denote Sobolev spaces and their norms [23].

Following [4], we relax the constraint in (2) with two penalization terms which lead us to rewrite the Plane-strain Ambrosio-Tortorelli elasticity functional as

$$\begin{aligned} J^{PAT}(\mathbf{u}, v) = & \frac{1}{2} \int_{\Omega} (v^2 + \eta) \sigma(\mathbf{u}) : E(\mathbf{u}) \, d\mathbf{x} + \frac{1}{2} \int_{\Omega} [\alpha(v-1)^2 + \varepsilon |\nabla v|^2] \, d\mathbf{x} \\ & + \frac{1}{2\gamma_A} \int_{\Omega_D} |\mathbf{u} - \mathbf{g}(t_k)|^2 \, d\mathbf{x} + \frac{1}{2\gamma_B} \int_{CR_{k-1}} v^2 \, d\mathbf{x}, \end{aligned} \quad (3)$$

where γ_A and γ_B are the penalty constants. Henceforth we always deal with this functional instead of (1). We are dealing now with an unconstrained minimization process. At each time level, we seek the pair $(\mathbf{u}(t_k), v(t_k))$ such that

$$(\mathbf{u}(t_k), v(t_k)) \in \underset{(\mathbf{u}, v) \in [H^1(\Omega)]^2 \times H^1(\Omega; [0, 1])}{\operatorname{argmin}} J^{PAT}(\mathbf{u}, v). \quad (4)$$

Since the penalized constraints are clearly continuous, convex, and always non-negative, the proof of the convergence of the minimizers of (4) to the minimizers of (2), for $\gamma_A, \gamma_B \rightarrow 0$, follows from Γ -convergence arguments (see [14]). Moreover, we are interested in local minimizers for two reasons. On the one side, the search for global minimizers is an NP-hard problem; on the other side, one can expect that the fracture moves along critical points of the physical energy. Therefore, it is not only (numerically) impossible to compute global minimizers with some guarantees, but it may also not be a meaningful choice from a physical viewpoint.

Mimicking the proof in [8] for the anti-plane case, we can prove that the functional J^{PAT} is Fréchet-differentiable in $[H^1(\Omega)]^2 \times (H^1(\Omega) \cap L^\infty(\Omega))$. In particular, the Fréchet derivative of J^{PAT} along direction (\mathbf{w}, z) is

$$\begin{aligned} (J^{PAT}(\mathbf{u}, v; \mathbf{w}, z))' = & \underbrace{\int_{\Omega} (v^2 + \eta) \sigma(\mathbf{u}) : E(\mathbf{w}) \, d\mathbf{x} + \frac{1}{\gamma_A} \int_{\Omega_D} (\mathbf{u} - \mathbf{g}(t_k)) \cdot \mathbf{w} \, d\mathbf{x}}_{=a(v; \mathbf{u}, \mathbf{w})} \\ & + \underbrace{\int_{\Omega} \left[v z \sigma(\mathbf{u}) : E(\mathbf{u}) + \alpha(v-1)z + \varepsilon \nabla v \cdot \nabla z \right] \, d\mathbf{x} + \frac{1}{\gamma_B} \int_{CR_{k-1}} v z \, d\mathbf{x}}_{=b(\mathbf{u}, v, z)}. \end{aligned} \quad (5)$$

Accordingly, we recall the definition of critical points of J^{PAT} :

Definition 1.1 *The pair $(\mathbf{u}, v) \in [H^1(\Omega)]^2 \times (H^1(\Omega) \cap L^\infty(\Omega))$ is a critical point of J^{PAT} if $(J^{PAT}(\mathbf{u}, v; \mathbf{w}, z))' = 0$ for all $\mathbf{w} \in [H^1(\Omega)]^2$ and for all $z \in (H^1(\Omega) \cap L^\infty(\Omega))$.*

Following Proposition 2.2 in [4], we can prove that condition $0 \leq v \leq 1$ is automatically guaranteed for any critical point.

2 Anisotropic Error Analysis

This section collects the main developments of this paper. After providing the discrete approximation of the functional J^{PAT} , we introduce the main tools of the anisotropic background, and we derive the theoretical result used to drive the anisotropic mesh adaptation procedure.

2.1 Discretization of J^{PAT}

We introduce the discrete counterpart of the minimization problem (4) in a finite element setting. Thus, we denote by $\{\mathcal{T}_h\}$ a family of conforming meshes of $\bar{\Omega}$, and let N_h be the index set of the vertices of \mathcal{T}_h , and \mathcal{E}_h the skeleton of \mathcal{T}_h . Henceforth, we assume that the boundary of Ω_D coincides with the union of consecutive edges in \mathcal{E}_h . We associate with \mathcal{T}_h the space X_h of continuous piecewise linear finite elements [11].

We denote by $J_h^{PAT}(\mathbf{u}_h, v_h)$ the discrete correspondent of $J^{PAT}(\mathbf{u}, v)$ in (3), with $\mathbf{u}_h = (u_{h,1}, u_{h,2})^T \in [X_h]^2$ and $v_h \in X_h$, given by

$$\begin{aligned} & J_h^{PAT}(\mathbf{u}_h, v_h) \\ &= \frac{1}{2} \int_{\Omega} \left[(P_h(v_h^2) + \eta) \sigma(\mathbf{u}_h) : E(\mathbf{u}_h) + \alpha P_h((v_h - 1)^2) + \varepsilon |\nabla v_h|^2 \right] dx \\ &+ \frac{1}{2\gamma_A} \sum_{i=1}^2 \int_{\Omega_D} P_h((u_{h,i} - g_{h,i}(t_k))^2) dx + \frac{1}{2\gamma_B} \int_{CR_{k-1}} P_h(v_h^2) dx, \end{aligned} \quad (6)$$

where $P_h : C^0(\bar{\Omega}) \rightarrow X_h$ is the Lagrangian interpolant onto the space X_h , with $\mathbf{g}_h(t_k) = (g_{h,1}(t_k), g_{h,2}(t_k))^T \in [X_h]^2$ a suitable discrete approximation of $\mathbf{g}(t_k)$. In particular, we pick $\mathbf{g}_h(t_k)$ such that

$$\int_{\Omega_D} \mathbf{g}_h(t_k) \cdot \mathbf{w}_h dx = \int_{\Omega_D} \mathbf{g}(t_k) \cdot \mathbf{w}_h dx \quad \forall \mathbf{w}_h \in [X_h]^2, \quad (7)$$

i.e., $\mathbf{g}_h(t_k)$ is the $L^2(\Omega_D)$ -projection of $\mathbf{g}(t_k)$ onto $[X_h]^2$. The action of the operator P_h is equivalent to a mass lumping [30].

The discrete analogue to (4) consists of finding the pair $(\mathbf{u}_h(t_k), v_h(t_k))$ such that

$$(\mathbf{u}_h(t_k), v_h(t_k)) \in \underset{(\mathbf{u}_h, v_h) \in [X_h]^2 \times X_h}{\operatorname{argmin}} J_h^{PAT}(\mathbf{u}_h, v_h).$$

Definition 1.1 can be also provided in the discrete case.

Definition 2.1 The pair $(\mathbf{u}_h, v_h) \in [X_h]^2 \times X_h$ is a critical point of J_h^{PAT} if, for all $(\mathbf{w}_h, z_h) \in [X_h]^2 \times X_h$, $(J_h^{PAT}(\mathbf{u}_h, v_h; \mathbf{w}_h, z_h))' = 0$, where

$$\begin{aligned} & (J_h^{PAT}(\mathbf{u}_h, v_h; \mathbf{w}_h, z_h))' = \\ & \underbrace{\int_{\Omega} (P_h(v_h^2) + \eta)\sigma(\mathbf{u}_h) : E(\mathbf{w}_h) \, d\mathbf{x} + \frac{1}{\gamma_A} \sum_{i=1}^2 \int_{\Omega_D} P_h((u_{h,i} - g_{h,i}(t_k))w_{h,i}) \, d\mathbf{x}}_{=a_h(v_h; \mathbf{u}_h, \mathbf{w}_h)} \\ & + \underbrace{\int_{\Omega} [P_h(v_h z_h)\sigma(\mathbf{u}_h) : E(\mathbf{u}_h) + \alpha P_h((v_h - 1)z_h) + \varepsilon \nabla v_h \cdot \nabla z_h] \, d\mathbf{x}}_{=} \\ & + \underbrace{\frac{1}{\gamma_B} \int_{CR_{k-1}} P_h(v_h z_h) \, d\mathbf{x}}_{=b_h(\mathbf{u}_h; v_h, z_h)} \end{aligned}$$

is the Fréchet derivative of J_h^{PAT} .

Thanks to the mass lumping associated with P_h and to the assumption

$$k_{ij} = \int_{\Omega} \nabla \xi_i \cdot \nabla \xi_j \, d\mathbf{x} \leq 0 \quad \forall i \neq j \in N_h,$$

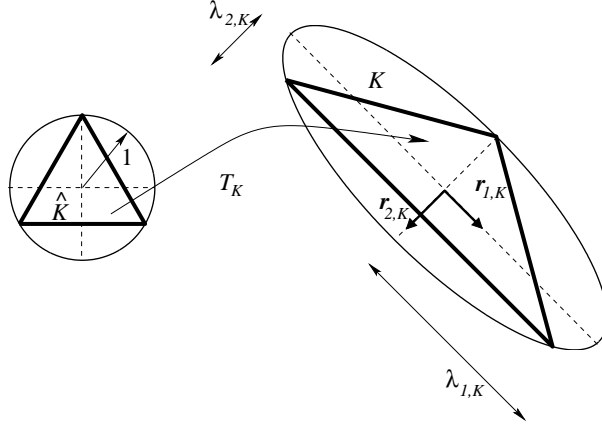
about the stiffness matrix K , with $\{\xi_l\}_{l=1}^{\#N_h}$ the basis of X_h , the property $0 \leq v_h \leq 1$, related to the discrete maximum principle (see, e.g., [12, 22, 29]), can be assessed for any critical point v_h of (6).

2.2 The Anisotropic Setting

Following [15, 25], we recover the anisotropic information from the spectral properties of the affine map $T_K : \widehat{K} \rightarrow K$, with $\mathbf{x} = T_K(\widehat{\mathbf{x}}) = M_K \widehat{\mathbf{x}} + \mathbf{b}_K$, from the equilateral reference triangle \widehat{K} with vertices $(-\sqrt{3}/2, -1/2)$, $(\sqrt{3}/2, -1/2)$, $(0, 1)$, inscribed in the unit circle, to the generic triangle K of \mathcal{T}_h , with $M_K \in \mathbb{R}^{2 \times 2}$, $\mathbf{b}_K \in \mathbb{R}^2$, $\mathbf{x} \in K$ and $\widehat{\mathbf{x}} \in \widehat{K}$.

In particular, we apply the polar decomposition to the Jacobian M_K , i.e., $M_K = B_K Z_K$, where $B_K, Z_K \in \mathbb{R}^{2 \times 2}$ are a symmetric positive definite and an orthogonal matrix, respectively. Matrix B_K deforms K , while Z_K turns it about the origin. Then, we consider the spectral decomposition of B_K , i.e., $B_K = R_K^T \Lambda_K R_K$, with $R_K^T = [\mathbf{r}_{1,K}, \mathbf{r}_{2,K}]$ and $\Lambda_K = \text{diag}(\lambda_{1,K}, \lambda_{2,K})$, with $\lambda_{1,K} \geq \lambda_{2,K}$. The eigenvectors $\mathbf{r}_{i,K}$ identify the directions of the semi-axes of the ellipse circumscribed to K , while the eigenvalues $\lambda_{i,K}$ provide the length of these semi-axes (see Fig. 1). We also define the aspect ratio of the element K by $s_K = \lambda_{1,K}/\lambda_{2,K}$. The value $s_K = 1$ corresponds to the isotropic case.

To derive the *a posteriori* error estimator, we introduce anisotropic error estimates for the quasi-interpolant Clément operator $\mathcal{C}_h : L^2(\Omega) \rightarrow X_h$ [13].

Figure 1: Anisotropic geometric quantities associated with the map T_K

Lemma 2.1 *Let $w \in H^1(\Omega)$. If $\#\Delta_K \leq \mathcal{N}$ for some $\mathcal{N} \in \mathbb{N}$, and $\text{diam}(T_K^{-1}(\Delta_K)) \leq C_\Delta \simeq O(1)$, where $\Delta_K = \{T \in \mathcal{T}_h : T \cap K \neq \emptyset\}$, then there exist constants $C_s = C_s(\mathcal{N}, C_\Delta)$, with $s = 1, 2, 3$, such that, for any $K \in \mathcal{T}_h$, it holds*

$$\begin{aligned} \|w - \mathcal{C}_h(w)\|_{L^2(K)} &\leq C_1 \left[\sum_{j=1}^2 \lambda_{j,K}^2 (\mathbf{r}_{j,K}^T G_{\Delta_K}(w) \mathbf{r}_{j,K}) \right]^{1/2}, \\ |w - \mathcal{C}_h(w)|_{H^1(K)} &\leq C_2 \frac{1}{\lambda_{2,K}} \left[\sum_{j=1}^2 \lambda_{j,K}^2 (\mathbf{r}_{j,K}^T G_{\Delta_K}(w) \mathbf{r}_{j,K}) \right]^{1/2}, \\ \|w - \mathcal{C}_h(w)\|_{L^2(\partial K)} &\leq C_3 \left(\frac{h_K}{\lambda_{1,K} \lambda_{2,K}} \right)^{1/2} \left[\sum_{j=1}^2 \lambda_{j,K}^2 (\mathbf{r}_{j,K}^T G_{\Delta_K}(w) \mathbf{r}_{j,K}) \right]^{1/2}, \end{aligned} \quad (8)$$

where $h_K = \text{diam}(K)$, while $G_{\Delta_K}(w)$ is the symmetric positive semi-definite matrix

$$G_{\Delta_K}(w) = \sum_{T \in \Delta_K} \begin{bmatrix} \int_T \left(\frac{\partial w}{\partial x_1} \right)^2 d\mathbf{x} & \int_T \frac{\partial w}{\partial x_1} \frac{\partial w}{\partial x_2} d\mathbf{x} \\ \int_T \frac{\partial w}{\partial x_1} \frac{\partial w}{\partial x_2} d\mathbf{x} & \int_T \left(\frac{\partial w}{\partial x_2} \right)^2 d\mathbf{x} \end{bmatrix}. \quad (9)$$

We refer to [17, 18] for the proof.

Osservazione 2.1 *The geometric hypotheses in Lemma 2.1 do not limit the anisotropic features of the elements, but ensure that the variation of these features is smooth over Δ_K [27].*

An equivalence result between the $H^1(\Delta_K)$ -seminorm and a corresponding anisotropic version is also useful for the *a posteriori* analysis.

Lemma 2.2 *Let $w \in H^1(\Omega)$ and $K \in \mathcal{T}_h$. For any $\beta_1, \beta_2 > 0$, it holds*

$$\min\{\beta_1, \beta_2\} \leq \frac{\beta_1(\mathbf{r}_{1,K}^T G_{\Delta_K}(w) \mathbf{r}_{1,K}) + \beta_2(\mathbf{r}_{2,K}^T G_{\Delta_K}(w) \mathbf{r}_{2,K})}{|w|_{H^1(\Delta_K)}^2} \leq \max\{\beta_1, \beta_2\},$$

where $G_{\Delta_K}(\cdot)$ is defined as in (9).

The proof of this result can be found in [24].

We have now all the theoretical tools required for tackling the anisotropic *a posteriori* analysis.

2.3 The *a Posteriori* Error Estimator

The following proposition states the main result of the paper and provides a variant on the anti-plane case addressed in [4].

Proposition 2.1 *Let $(\mathbf{u}_h, v_h) \in [X_h]^2 \times X_h$ be a critical point of J_h^{PAT} according to Definition 2.1. Then, for any pair of functions $(\mathbf{w}, z) \in [H^1(\Omega)]^2 \times H^1(\Omega)$, with $\mathbf{w} = (w_1, w_2)^T$, it holds*

$$|(J^{PAT}(\mathbf{u}_h, v_h; \mathbf{w}, z))'| \leq C \sum_{K \in \mathcal{T}_h} \left\{ \sum_{i=1}^2 \rho_{i,K}^A(v_h, \mathbf{u}_h) \omega_K(w_i) + \rho_K^B(\mathbf{u}_h, v_h) \omega_K(z) \right\}, \quad (10)$$

where $C = C(\mathcal{N}, C_\Delta)$, the residuals $\rho_{i,K}^A(v_h, \mathbf{u}_h)$ and $\rho_K^B(\mathbf{u}_h, v_h)$ are

$$\begin{aligned} \rho_{i,K}^A(v_h, \mathbf{u}_h) &= \|2v_h \sigma_i(\mathbf{u}_h) \cdot \nabla v_h\|_{L^2(K)} + \frac{1}{\lambda_{2,K}} \|v_h^2 - P_h(v_h^2)\|_{L^\infty(K)} \|\sigma_i(\mathbf{u}_h)\|_{L^2(K)} \\ &+ \frac{1}{2} \|\sigma_i(\mathbf{u}_h)\|_{L^\infty(\partial K)} \|v_h^2 + \eta\|_{L^2(\partial K)} \left(\frac{h_K}{\lambda_{1,K} \lambda_{2,K}} \right)^{1/2} + \frac{|K|^{1/2} h_K^2}{\lambda_{2,K} \gamma_A} |u_{h,i} - g_{h,i}(t_k)|_{W^{1,\infty}(K)} \\ &+ \frac{\delta_{K,\Omega_D}}{\gamma_A} (\|u_{h,i} - g_{h,i}(t_k)\|_{L^2(K)} + \|g_{h,i}(t_k) - g_i(t_k)\|_{L^2(K)}), \end{aligned}$$

$$\begin{aligned} \rho_K^B(\mathbf{u}_h, v_h) &= \|(\sigma(\mathbf{u}_h) : E(\mathbf{u}_h) + \alpha)v_h - \alpha\|_{L^2(K)} + \frac{\varepsilon}{2} \|\llbracket \nabla v_h \rrbracket\|_{L^2(\partial K)} \left(\frac{h_K}{\lambda_{1,K} \lambda_{2,K}} \right)^{1/2} \\ &+ \frac{\delta_{K,CR_{k-1}}}{\gamma_B} \|v_h\|_{L^2(K)} + \frac{h_K^2}{\lambda_{2,K}} \left[\|\sigma(\mathbf{u}_h) : E(\mathbf{u}_h) + \alpha\|_{L^2(K)} + \frac{|K|^{1/2} \delta_{K,CR_{k-1}}}{\gamma_B} \right] |v_h|_{W^{1,\infty}(K)}, \end{aligned}$$

with $\mathbf{u}_h = (u_{h,1}, u_{h,2})^T$, the weights are

$$\omega_K(\xi) = \left[\sum_{i=j}^2 \lambda_{j,K}^2 (\mathbf{r}_{j,K}^T G_{\Delta_K}(\xi) \mathbf{r}_{j,K}) \right]^{1/2} \quad \forall \xi \in H^1(\Omega),$$

where

$$[[\sigma_i(\mathbf{u}_h)]] = \begin{cases} [\sigma_i(\mathbf{u}_h) \cdot \mathbf{n}]_e & e \in \mathcal{E}_h \cap \Omega \\ 2(\sigma_i(\mathbf{u}_h) \cdot \mathbf{n})|_e & e \in \mathcal{E}_h \cap \partial\Omega \end{cases}, \quad (11)$$

$$[[\nabla v_h]] = \begin{cases} [\nabla v_h \cdot \mathbf{n}]_e & e \in \mathcal{E}_h \cap \Omega \\ 2(\nabla v_h \cdot \mathbf{n})|_e & e \in \mathcal{E}_h \cap \partial\Omega \end{cases} \quad (12)$$

denote the generalized jump of the i -th component of the normal Cauchy stress tensor and of the normal derivative of v_h , respectively, with $[\cdot]_e$ the standard jump across e , \mathbf{n} the unit normal vector to the generic edge in \mathcal{E}_h , $\sigma_i(\mathbf{u}_h)$ the i -th column of σ , \mathbf{g}_h is chosen as in (7), and $\delta_{K,\varpi} = 1$ if $K \cap \varpi \neq \emptyset$ and $\delta_{K,\varpi} = 0$ otherwise, with $\varpi \subset \Omega$.

Proof. Since (\mathbf{u}_h, v_h) is a critical point of J_h^{PAT} , we have that

$$a_h(v_h; \mathbf{u}_h, \mathbf{w}_h) = 0 \quad \forall \mathbf{w}_h \in [X_h]^2, \quad b_h(\mathbf{u}_h; v_h, z_h) = 0 \quad \forall z_h \in X_h. \quad (13)$$

Moreover, from (5), for any pair $(\mathbf{w}, z) \in [H^1(\Omega)]^2 \times H^1(\Omega)$, it holds

$$|(J_h^{PAT}(\mathbf{u}_h, v_h; \mathbf{w}, z))'| \leq |a(v_h; \mathbf{u}_h, \mathbf{w})| + |b(\mathbf{u}_h; v_h, z)|. \quad (14)$$

Now, we analyze the two terms in (14) separately, starting from $|a(v_h; \mathbf{u}_h, \mathbf{w})|$. Thanks to (13), for any $\mathbf{w} \in [H^1(\Omega)]^2$ and $\mathbf{w}_h \in [X_h]^2$, we have that

$$|a(v_h; \mathbf{u}_h, \mathbf{w})| \leq |a(v_h; \mathbf{u}_h, \mathbf{w} - \mathbf{w}_h)| + |a(v_h; \mathbf{u}_h, \mathbf{w}_h) - a_h(v_h; \mathbf{u}_h, \mathbf{w}_h)|. \quad (15)$$

Let us focus on the first term on the right-hand side of (15). After splitting the integrals on the mesh elements, and by exploiting integration by parts, we get

$$\begin{aligned} |a(v_h; \mathbf{u}_h, \mathbf{w} - \mathbf{w}_h)| &= \left| \sum_{K \in \mathcal{T}_h} \left\{ \int_K (v_h^2 + \eta) \sigma(\mathbf{u}_h) : E(\mathbf{w} - \mathbf{w}_h) \, d\mathbf{x} \right. \right. \\ &\quad \left. \left. + \frac{1}{\gamma_A} \int_K (\mathbf{u}_h - \mathbf{g}(t_k)) \cdot (\mathbf{w} - \mathbf{w}_h) \chi_{\Omega_D} \, d\mathbf{x} \right\} \right| \\ &= \left| \sum_{K \in \mathcal{T}_h} \left\{ \int_K -2v_h \sigma(\mathbf{u}_h) (\mathbf{w} - \mathbf{w}_h) \cdot \nabla v_h \, d\mathbf{x} + \int_{\partial K} (v_h^2 + \eta) \sigma(\mathbf{u}_h) (\mathbf{w} - \mathbf{w}_h) \cdot \mathbf{n} \, ds \right. \right. \\ &\quad \left. \left. + \frac{1}{\gamma_A} \int_K [(\mathbf{u}_h - \mathbf{g}_h(t_k)) + (\mathbf{g}_h(t_k) - \mathbf{g}(t_k))] \cdot (\mathbf{w} - \mathbf{w}_h) \chi_{\Omega_D} \, d\mathbf{x} \right\} \right|, \end{aligned}$$

where χ_ϖ denotes the characteristic function of the generic set $\varpi \subset \Omega$. To preserve the directional information, we now deal with the terms on the right-hand side componentwise. For this purpose, we define

$$a(v_h; \mathbf{u}_h, \mathbf{w} - \mathbf{w}_h) = \sum_{i=1}^2 a_i(v_h; \mathbf{u}_h, w_i - w_{h,i}),$$

with $\mathbf{w}_h = (w_{h,1}, w_{h,2})^T$, and

$$\begin{aligned} a_i(v_h; \mathbf{u}_h, w_i - w_{h,i}) &= \\ &\sum_{K \in \mathcal{T}_h} \left\{ \int_K -2v_h \sigma_i(\mathbf{u}_h) \cdot \nabla v_h (w_i - w_{h,i}) \, d\mathbf{x} + \int_{\partial K} (v_h^2 + \eta) \sigma_i(\mathbf{u}_h) \cdot \mathbf{n} (w_i - w_{h,i}) \, ds \right. \\ &\quad \left. + \frac{1}{\gamma_A} \int_K [(u_{h,i} - g_{h,i}(t_k)) + (g_{h,i}(t_k) - g_i(t_k))] (w_i - w_{h,i}) \chi_{\Omega_D} \, d\mathbf{x} \right\}. \end{aligned}$$

Thanks to Hölder and Cauchy-Schwarz inequalities and definition (11)-(12), we obtain

$$\begin{aligned} |a_i(v_h; \mathbf{u}_h, w_i - w_{h,i})| &\leq \sum_{K \in \mathcal{T}_h} \left\{ \|2v_h \sigma_i(\mathbf{u}_h) \cdot \nabla v_h\|_{L^2(K)} \|w_i - w_{h,i}\|_{L^2(K)} \right. \\ &+ \frac{1}{2} \|[\sigma_i(\mathbf{u}_h)]\|_{L^\infty(\partial K)} \|v_h^2 + \eta\|_{L^2(\partial K)} \|w_i - w_{h,i}\|_{L^2(\partial K)} + \frac{1}{\gamma_A} \|(w_i - w_{h,i}) \chi_{\Omega_D}\|_{L^2(K)} \\ &\left. \left(\|(u_{h,i} - g_{h,i}(t_k)) \chi_{\Omega_D}\|_{L^2(K)} + \|(g_{h,i}(t_k) - g_i(t_k)) \chi_{\Omega_D}\|_{L^2(K)} \right) \right\}. \end{aligned}$$

Picking $w_{h,i} = \mathcal{C}_h(w_i)$ and thanks to Lemma 2.1, we obtain

$$\begin{aligned} |a_i(v_h; \mathbf{u}_h, w_i - w_{h,i})| &\leq C \sum_{K \in \mathcal{T}_h} \left\{ \|2v_h \sigma_i(\mathbf{u}_h) \cdot \nabla v_h\|_{L^2(K)} \right. \\ &+ \frac{1}{2} \|[\sigma_i(\mathbf{u}_h)]\|_{L^\infty(\partial K)} \|v_h^2 + \eta\|_{L^2(\partial K)} \left(\frac{h_K}{\lambda_{1,K} \lambda_{2,K}} \right)^{1/2} + \frac{\delta_{K,\Omega_D}}{\gamma_A} \\ &\left. \left(\|u_{h,i} - g_{h,i}(t_k)\|_{L^2(K)} + \|g_{h,i}(t_k) - g_i(t_k)\|_{L^2(K)} \right) \right\} \left[\sum_{j=1}^2 \lambda_{j,K}^2 (\mathbf{r}_{j,K}^T G_{\Delta_K}(w_i) \mathbf{r}_{j,K}) \right]^{1/2}. \end{aligned} \quad (16)$$

Now we deal with the second term on the right-hand side of (15), that we bound as

$$\begin{aligned} |a(v_h; \mathbf{u}_h, \mathbf{w}_h) - a_h(v_h; \mathbf{u}_h, \mathbf{w}_h)| &\leq \left| \int_{\Omega} [v_h^2 - P_h(v_h^2)] \sigma(\mathbf{u}_h) : E(\mathbf{w}_h) \, d\mathbf{x} \right| \\ &+ \frac{1}{\gamma_A} \left| \int_{\Omega_D} (I - P_h)((\mathbf{u}_h - \mathbf{g}_h(t_k)) \cdot \mathbf{w}_h) \, d\mathbf{x} \right| + \frac{1}{\gamma_A} \left| \int_{\Omega_D} (\mathbf{g}_h(t_k) - \mathbf{g}(t_k)) \cdot \mathbf{w}_h \, d\mathbf{x} \right|. \end{aligned} \quad (17)$$

We anticipate the auxiliary result based on the equivalence of norms on a finite-dimensional space,

$$|\varphi_h \psi_h|_{H^2(K)} \leq 4 |\varphi_h|_{W^{1,\infty}(K)} \|\nabla \psi_h\|_{L^2(K)} \quad \forall \varphi_h, \psi_h \in X_h, \quad \forall K \in \mathcal{T}_h, \quad (18)$$

which follows by straightforward calculus. Using the definition (7) of $\mathbf{g}_h(t_k)$, the last term in (17) turns out to be zero. Considering again (17) componentwise, employing Hölder and Cauchy-Schwarz inequalities together with the standard isotropic estimate for the L^2 -norm of the interpolation error associated with P_h , we get

$$\begin{aligned} |a_i(v_h; \mathbf{u}_h, \mathbf{w}_h) - a_{i,h}(v_h; \mathbf{u}_h, \mathbf{w}_h)| &\leq C \sum_{K \in \mathcal{T}_h} \left\{ \frac{|K|^{1/2} h_K^2}{\gamma_A} |(u_{h,i} - g_{h,i}(t_k)) w_{h,i}|_{H^2(K)} \right. \\ &\left. + \|v_h^2 - P_h(v_h^2)\|_{L^\infty(K)} \|\sigma_i(\mathbf{u}_h)\|_{L^2(K)} \|\nabla w_{h,i}\|_{L^2(K)} \right\}, \end{aligned}$$

where the constant C does not depend on the aspect ratio s_K of K . Then, we employ (18) together with estimate (8) and Lemma 2.2 with $\beta_1 = \lambda_{1,K}^2$, $\beta_2 = \lambda_{2,K}^2$, to obtain

$$\begin{aligned}
& |a_i(v_h; u_h, \mathbf{w}_h) - a_{i,h}(v_h; u_h, \mathbf{w}_h)| \leq C \sum_{K \in \mathcal{T}_h} \left\{ \left(\frac{|K|^{1/2} h_K^2}{\gamma_A} |u_{h,i} - g_{h,i}(t_k)|_{W^{1,\infty}(K)} \right. \right. \\
& \left. \left. + \|v_h^2 - P_h(v_h^2)\|_{L^\infty(K)} \|\sigma_i(\mathbf{u}_h)\|_{L^2(K)} \right) \|\nabla w_{h,i}\|_{L^2(K)} \right\} \\
& \leq C \sum_{K \in \mathcal{T}_h} \left\{ \left(\frac{|K|^{1/2} h_K^2}{\gamma_A} |u_{h,i} - g_{h,i}(t_k)|_{W^{1,\infty}(K)} + \|v_h^2 - P_h(v_h^2)\|_{L^\infty(K)} \|\sigma_i(\mathbf{u}_h)\|_{L^2(K)} \right) \right. \\
& \quad \left. \left(\|\nabla w_{h,i} - \nabla w_i\|_{L^2(K)} + \|\nabla w_i\|_{L^2(K)} \right) \right\} \\
& \leq C \sum_{K \in \mathcal{T}_h} \left\{ \left(\frac{|K|^{1/2} h_K^2}{\gamma_A} |u_{h,i} - g_{h,i}(t_k)|_{W^{1,\infty}(K)} + \|v_h^2 - P_h(v_h^2)\|_{L^\infty(K)} \|\sigma_i(\mathbf{u}_h)\|_{L^2(K)} \right) \right. \\
& \quad \left. \frac{1}{\lambda_{2,K}} \left[\sum_{j=1}^2 \lambda_{j,K}^2 (\mathbf{r}_{j,K}^T G_{\Delta_K}(w_i) \mathbf{r}_{j,K}) \right]^{1/2} \right\}.
\end{aligned} \tag{19}$$

Therefore, collecting (16) and (19), we are able to bound componentwise the first term on the right-hand side of (14), as

$$|a(v_h; \mathbf{u}_h, \mathbf{w})| \leq C \sum_{K \in \mathcal{T}_h} \sum_{i=1}^2 \rho_{i,K}^A(v_h, \mathbf{u}_h) \omega_K^A(w_i).$$

The estimate of the second term on the right-hand side of (14) can be carried out exactly as the corresponding one in the proof of Proposition 3.3 in [4], after replacing $|\nabla u_h|^2$ with $\sigma(\mathbf{u}_h) : E(\mathbf{u}_h)$. This yields

$$4|b(\mathbf{u}_h; v_h, z)| \leq C \sum_{K \in \mathcal{T}_h} \rho_K^B(\mathbf{u}_h, v_h) \omega_K(z).$$

□

To make estimate (10) useful in practice, we have to pick the pair of functions (\mathbf{w}, z) . Mimicking the considerations in [4], we choose $\mathbf{w} = \mathbf{u}_h$ and $z = v_h$. This leads us to define the error estimator

$$\eta = \sum_{K \in \mathcal{T}_h} \eta_K(\mathbf{u}_h, v_h),$$

where the local estimator is

$$\eta_K(\mathbf{u}_h, v_h) = \sum_{i=1}^2 \rho_{i,K}^A(v_h, \mathbf{u}_h) \omega_K(u_{h,i}) + \rho_K^B(\mathbf{u}_h, v_h) \omega_K(v_h). \tag{20}$$

Osservazione 2.2 *Although in this work we deal with a specific case of linear elasticity constitutive law, we do believe that it is possible to extend the a posteriori analysis to a more general model, for instance, the one recently introduced in [9].*

3 The Numerical Anisotropic Procedure

The numerical minimization of (6) is not a trivial task since it is a nonconvex functional due to the presence of the term $P_h(v_h^2)\sigma(\mathbf{u}_h) : E(\mathbf{u}_h)$. In particular, the methods available in the literature do not guarantee, in general, the convergence to global minimizers (see, e.g., [5]) but only to local minima.

In the first part of this section, we introduce the procedure exploited to convert the anisotropic estimator (20) into an actual anisotropic tool. In the second part of this section, we merge this approach with a suitable minimization algorithm, extending the method in [4].

3.1 A Metric-Driven Approach

Following [15, 25], we use a metric-based mesh adaptive approach (see, e.g., [20]). In particular, we predict the mesh with the least number of elements ensuring a given accuracy on the global estimator η .

There exists a tight relation between metric and mesh. Actually, with an assigned mesh \mathcal{T}_h , we can associate a corresponding piecewise constant metric given by $M_K = R_K^T \Lambda_K^{-2} R_K$, for any $K \in \mathcal{T}_h$, where matrices R_K and Λ_K are exactly the same as in Sect. 2.2. Likewise, for a given metric field $\mathcal{M} : \Omega \rightarrow \mathbb{R}^{2 \times 2}$, we can build a mesh, say $\mathcal{T}_{\mathcal{M}}$, such that $\mathcal{M}_K = \mathcal{M}|_K$ coincides with M_K , for any $K \in \mathcal{T}_{\mathcal{M}}$.

To build the new adapted mesh, we adopt a two-step procedure. First, we derive a metric \mathcal{M} out of the error estimator (20). Then, we generate the new mesh induced by this metric using the metric-based mesh generator in `FreeFem++` [21].

To obtain \mathcal{M} , we resort to an iterative procedure. At each iteration, say l , we deal with three quantities:

- i) the actual mesh $\mathcal{T}_h^{(l)}$;
- ii) the new metric $\mathcal{M}^{(l+1)}$ computed on $\mathcal{T}_h^{(l)}$;
- iii) the updated mesh $\mathcal{T}_h^{(l+1)}$ induced by $\mathcal{M}^{(l+1)}$.

The new metric is predicted by suitably rewriting the local estimator $\eta_K(\mathbf{u}_h, v_h)$ to single out the geometric information and then by applying an error equidistribution criterion combined with the minimization of the number of elements. The re-arranged local estimator is

$$\eta_K(\mathbf{u}_h, v_h) = \mu_K \left\{ \sum_{i=1}^2 \bar{\rho}_{i,K}^A(v_h, \mathbf{u}_h) \bar{\omega}_K(u_{h,i}) + \bar{\rho}_K^B(\mathbf{u}_h, v_h) \bar{\omega}_K(v_h) \right\}, \quad (21)$$

where $\mu_K = |\widehat{K}| (\lambda_{1,K} \lambda_{2,K})^{3/2}$ lumps all the area $|K|$ information,

$$\bar{\rho}_{i,K}^A(v_h, \mathbf{u}_h) = \frac{\rho_{i,K}^A(v_h, \mathbf{u}_h)}{(|\widehat{K}| \lambda_{1,K} \lambda_{2,K})^{1/2}}, \quad \bar{\rho}_K^B(\mathbf{u}_h, v_h) = \frac{\rho_K^B(\mathbf{u}_h, v_h)}{(|\widehat{K}| \lambda_{1,K} \lambda_{2,K})^{1/2}},$$

with $i = 1, 2$, are approximately pointwise values (at least for a sufficiently fine mesh), while the anisotropic information associated with K is collected in the scaled weights

$$\bar{\omega}_K(\xi_h) = \left[s_K \mathbf{r}_{1,K}^T \bar{G}_{\Delta_K}(\xi_h) \mathbf{r}_{1,K} + \frac{1}{s_K} \mathbf{r}_{2,K}^T \bar{G}_{\Delta_K}(\xi_h) \mathbf{r}_{2,K} \right]^{1/2},$$

with $\xi_h = u_{h,1}, u_{h,2}, v_h$, and $\bar{G}_{\Delta_K}(\cdot) = G_{\Delta_K}(\cdot)/(|\hat{K}| \lambda_{1,K} \lambda_{2,K})$. In principle, each term in (21) provides a metric. For practical reasons, however, we merge this information to obtain a single metric, thus avoiding metric intersection. To do this, we follow the approach in Sect. 4 of [26], which allows us to rewrite (21) as

$$\eta_K(\mathbf{u}_h, v_h) = \mu_K \Upsilon_K$$

with

$$\Upsilon_K = \left[s_K \mathbf{r}_{1,K}^T \Gamma_K \mathbf{r}_{1,K} + \frac{1}{s_K} \mathbf{r}_{2,K}^T \Gamma_K \mathbf{r}_{2,K} \right]^{1/2}, \quad (22)$$

where the local matrix

$$\Gamma_K = \sum_{i=1}^2 [\bar{\rho}_{i,K}^A(v_h, \mathbf{u}_h)]^2 \bar{G}_{\Delta_K}(u_{h,i}) + [\bar{\rho}_K^B(\mathbf{u}_h, v_h)]^2 \bar{G}_{\Delta_K}(v_h) \quad (23)$$

gathers the anisotropic information provided by \mathbf{u}_h and v_h , suitably weighted via the local residuals.

We minimize now the number of mesh elements by maximizing the area of each element K with an error *equidistribution* constraint, i.e., we enforce that, for each element $K \in \mathcal{T}_h^{(l+1)}$, $\eta_K(\mathbf{u}_h, v_h) = \mu_K \Upsilon_K = \text{TOL}/\#\mathcal{T}_h^{(l)}$, where TOL and $\#\mathcal{T}_h^{(l)}$ are the user-defined global tolerance and the number of mesh elements in $\mathcal{T}_h^{(l)}$, respectively. The constant value $\text{TOL}/\#\mathcal{T}_h^{(l)}$ is ensured with an element of maximal area only if Υ_K is minimized with respect to s_K and $\mathbf{r}_{1,K}$, i.e., we solve elementwise the constrained minimization problem

$$\min_{s_K \geq 1, \mathbf{r}_{m,K} \cdot \mathbf{r}_{n,K} = \delta_{mn}} \Upsilon_K(\mathbf{r}_{1,K}, s_K), \quad (24)$$

δ_{mn} being the Kronecker symbol. For computational convenience, all the quantities appearing in (23) are evaluated on the background grid $\mathcal{T}_h^{(l)}$. On the other hand, the aspect ratio s_K and the unit vector $\mathbf{r}_{1,K}$ in (22) represent our actual unknowns. According to Proposition 4.2 in [26], we can state the desired minimization result.

Proposition 3.1 *Let $\{\gamma_{i,K}, g_{i,K}\}$ be the eigenvector-eigenvalue pair of Γ_K with $g_{1,K} \geq g_{2,K} > 0$. Then, the minimum (24) is obtained for the choices*

$$\mathbf{r}_{1,K} = \gamma_{2,K} \quad \text{and} \quad s_K = \left(\frac{g_{1,K}}{g_{2,K}} \right)^{1/2}, \quad (25)$$

yielding the value $(2\sqrt{g_{1,K}g_{2,K}})^{1/2}$ for Υ_K .

The minimization problem (24) can be solved analytically via (25) without resorting to any numerical optimization tool.

Finally, the optimal metric $\mathcal{M}^{(l+1)}$ is generated by exploiting again the equidistribution constraint, i.e., by solving the equations

$$|\widehat{K}| (\lambda_{1,K} \lambda_{2,K})^{3/2} (2 \sqrt{g_{1,K} g_{2,K}})^{1/2} = \frac{\text{TOL}}{\#\mathcal{T}_h^{(l)}} \quad \text{and} \quad \frac{\lambda_{1,K}}{\lambda_{2,K}} = s_K = \left(\frac{g_{1,K}}{g_{2,K}} \right)^{1/2}. \quad (26)$$

System (26) provides us with the distinct values

$$\lambda_{1,K} = \left(\frac{1}{|\widehat{K}| \sqrt{2}} \left(\frac{g_{1,K}}{g_{2,K}^2} \right)^{1/2} \frac{\text{TOL}}{\#\mathcal{T}_h^{(l)}} \right)^{1/3}, \quad \lambda_{2,K} = \left(\frac{1}{|\widehat{K}| \sqrt{2}} \left(\frac{g_{2,K}}{g_{1,K}^2} \right)^{1/2} \frac{\text{TOL}}{\#\mathcal{T}_h^{(l)}} \right)^{1/3}. \quad (27)$$

Eventually, the optimal metric $\mathcal{M}^{(l+1)}$ is characterized by $\mathbf{r}_{1,K}$ in (25), $\lambda_{1,K}$ and $\lambda_{2,K}$ in (27), with $\mathbf{r}_{2,K} \perp \mathbf{r}_{1,K}$.

3.2 The Whole Adaptive Procedure

In this section we propose a numerical algorithm which combines a suitable minimization method for the nonconvex functional J_h^{PAT} with the mesh adaptation procedure of the previous section.

The algorithm is a generalization of the Algorithms 2 and 3 proposed in [4]. In practice, we switch from mesh adaptation, driven by the tolerance $\text{TOL} = \text{REFTOL} \ll 1$, to minimization of J_h^{PAT} , until both the mesh and the functional stagnate to within given thresholds, $\text{MESHTOL} \ll 1$ and $\text{VTOL} \ll 1$, respectively. The minimization of the functional exploits the alternate minimization algorithm proposed in [8] for dealing with nonconvex functionals, relying on the convexity only along the directions identified by \mathbf{u}_h and v_h . In particular, our new algorithm carries out mesh adaptation after a maximum number, \mathbf{nMIN} , of minimization steps. Given an initial mesh, $\mathcal{T}_h^{(0)}$, we proceed as follows: The minimization of the functional with respect to \mathbf{u}_h and v_h is performed by solving the corresponding Euler-Lagrange equations, since the functional is actually (strictly) convex with respect to the individual variables. In both cases, the equations are standard linear elliptic problems.

The interpolation operator $\Pi_{n \rightarrow n+1}(z_h)$ is used to map the finite element function z_h defined on \mathcal{T}_h^n onto the new mesh \mathcal{T}_h^{n+1} , before restarting any new optimization or time loop.

The convergence of the mesh adaptivity is assessed by checking the relative variation of the number of elements. The main novelty with respect to the algorithms in [4] is that, through \mathbf{nMIN} , the functional J_h^{PAT} is not necessarily exactly minimized after the inner **while** loop. Algorithms 2 and 3 represent particular cases of the algorithm above. Selecting $\mathbf{nMIN} = \infty$, we recover Algorithm 2, which is suited to deal with slowly advancing fractures, because the coupling between optimization and adaptation is not so tight. Setting $\mathbf{nMIN} = 1$,

we get back Algorithm 3, which alternates optimization and mesh adaptation more closely. However, in such a case, the crack evolution may be biased by the mesh which is adapted to nonoptimal fields, \mathbf{u}_h, v_h . These values of **nMIN** represent two extreme choices. In general, we may pick any intermediate value, e.g., **nMIN** = 7 in the section below.

Algorithm 3.1 Optimize(**nMIN**)-while-Adapt

```

1: Set  $k = 0, l = 0$ ;
2: If  $k = 0$ , set  $v_h^1 = 1$ ; else  $v_h^1 = v_h(t_{k-1})$ ;
3: Set  $l = 0$ ; errmesh = 1; err = 1;
4: while errmesh  $\geq$  MESHTOL | err  $\geq$  VTOL do
5:   Set  $i = 1$ ; err = 1;
6:   while err  $\geq$  VTOL &  $i \leq$  nMIN do
7:      $\mathbf{u}_h^i = \operatorname{argmin}_{\mathbf{z}_h \in [X_h^{(l)}]^2} J_h^{PAT}(\mathbf{z}_h, v_h^i)$ ;
8:      $v_h^{i+1} = \operatorname{argmin}_{z_h \in X_h^{(l)}} J_h^{PAT}(\mathbf{u}_h^i, z_h)$ ;
9:     err =  $\|v_h^{i+1} - v_h^i\|_{L^\infty(\Omega)}$ ;
10:     $i \leftarrow i + 1$ ;
11:   end while
12:   Compute the new metric  $\mathcal{M}^{(l+1)}$  based on  $\mathbf{u}_h^{i-1}$  and  $v_h^i$ ;
13:   Build the adapted mesh  $\mathcal{T}_h^{(l+1)}$ ;
14:   errmesh =  $|\#\mathcal{T}_h^{(l+1)} - \#\mathcal{T}_h^{(l)}| / \#\mathcal{T}_h^{(l)}$ ;
15:   Set  $v_h^1 = \Pi_{l \rightarrow l+1}(v_h^i)$ ;
16:    $l \leftarrow l + 1$ ;
17: end while
18:  $\mathbf{u}_h(t_k) = \Pi_{l-1 \rightarrow l}(\mathbf{u}_h^{i-1})$ ;  $v_h(t_k) = \Pi_{l-1 \rightarrow l}(v_h^i)$ ;  $\mathcal{T}_h^k = \mathcal{T}_h^{(l)}$ ;
19: Set  $\mathcal{T}_h^{(0)} = \mathcal{T}_h^k$ ;
20:  $k \leftarrow k + 1$ ;
21: if  $k > F$ , stop; else goto 2.

```

4 Numerical Assessment

We verify Algorithm 3.1 on two numerical tests inspired by [7, 16]. The second test case turns out to be particularly challenging.

4.1 Traction of a Fiber-Reinforced Matrix

We consider the rectangular domain $\Omega = (0, 3) \times (0, 3.5)$ in Fig. 2 left, comprising a nonelastic circular fiber of radius 0.5 centered at (1.5, 1.5), for $t \in [0, 0.5]$, uniformly partitioned with a total number of $F = 50$ time steps. On the subdomain $\Omega_D = (0, 3) \times (3, 3.5)$ we enforce the load \mathbf{g} , with $\mathbf{g}_D = (0, t)^T$. The fiber is held fixed while a uniform vertical displacement is induced by \mathbf{g}_D on the top side of

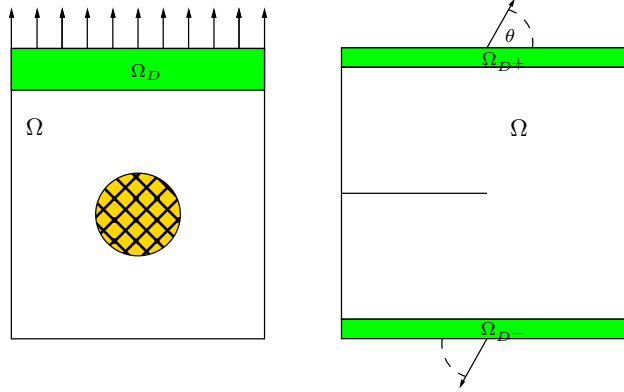


Figure 2: Geometric configurations for the traction of a fiber-reinforced matrix (left) and for the crack branching test (right)

the matrix. The other sides of the domain are traction-free. As a function of time, at the beginning the matrix behaves elastically; then, an asymmetric crack suddenly develops and eventually cuts the matrix in two parts. The parameters involved in (3) are set to

$$\varepsilon = 10^{-1}, \quad \eta = 10^{-3}, \quad \gamma_A = \gamma_B = 10^{-7}, \quad \lambda = \frac{Yp}{(1+p)(1-2p)}, \quad \mu = \frac{Y}{2(1+p)},$$

where $Y = 30$ is Young's modulus and $p = 0.18$ is the Poisson coefficient. The values of the tolerances required by Algorithm 3.1 are

$$\text{VTOL} = 5 \cdot 10^{-3}, \quad \text{CRTOL} = \text{REFTOL} = 10^{-3}, \quad \text{MESHTOL} = 10^{-2}.$$

Figure 3 shows the v_h -field at three time levels as well as the associated anisotropic adapted mesh. At time $t = 0.25$ a crack on top of the fiber is created and starts propagating slowly and symmetrically with respect to the fiber. At time $t = 0.35$ the symmetry is broken and the crack splits the matrix on one side only. Afterwards, at time $t = 0.39$, the domain is thoroughly split into two parts. This behavior is not essentially affected by ε . Actually, a reduction of this parameter by one order of magnitude yields the results in Fig. 4, which share the same pattern as in Fig. 3, although with a sharper crack. In all cases, the adapted meshes are very fine close to the fracture and in the area of higher stress. Moreover, the correct path of the crack is detected in a very efficient way, i.e., with quite few elements. In particular, in Fig. 3 and 4 (bottom-right), the meshes consist only of 1810 and 12381 elements, respectively. The maximum aspect ratio of the three meshes in Fig. 3 is 16, 32 and 109.

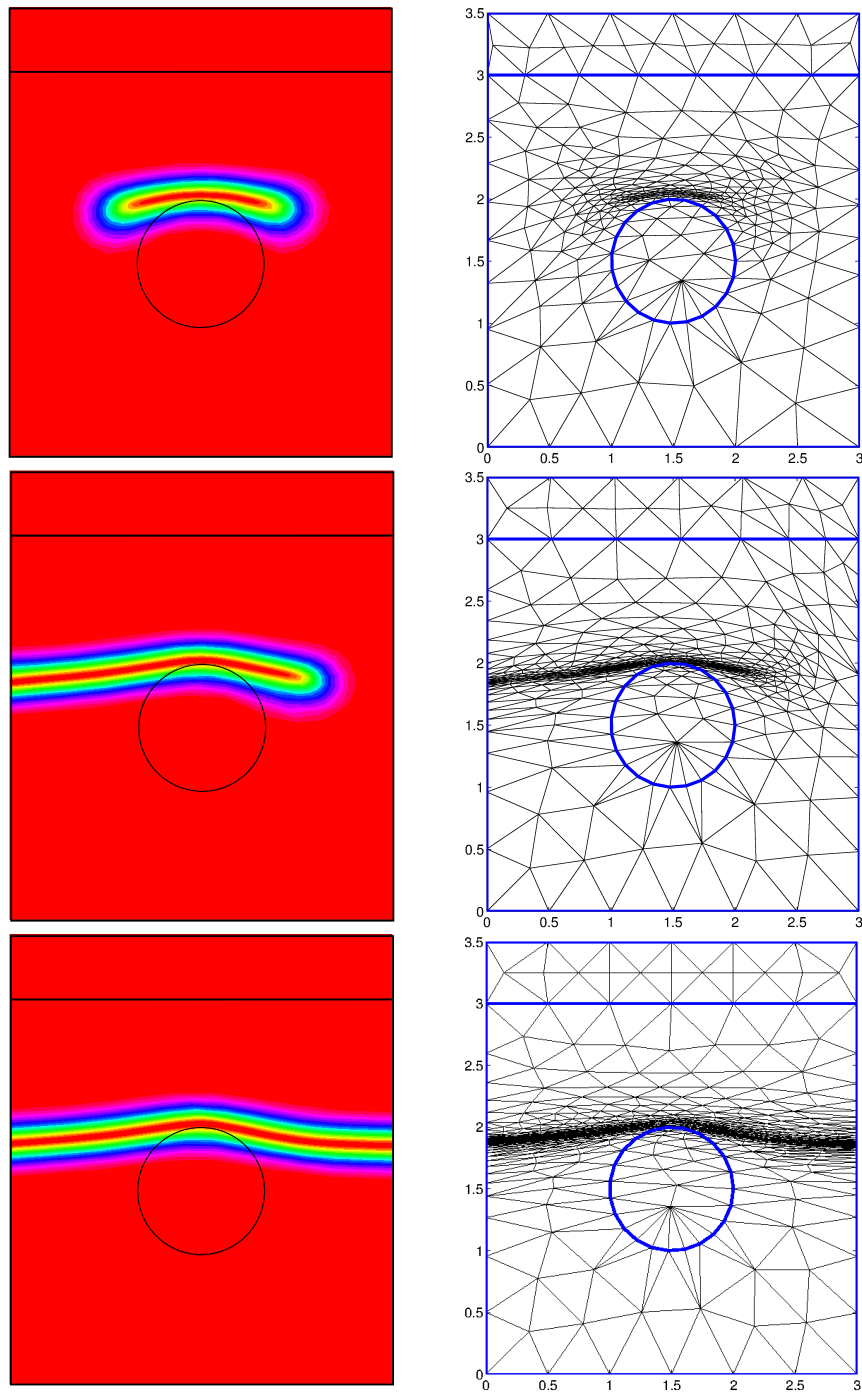


Figure 3: Traction of a fiber-reinforced matrix. Time evolution of the v_h -field (left): $t = 0.25$ (top), $t = 0.35$ (center), and $t = 0.39$ (bottom); corresponding adapted meshes (right) with $\varepsilon = 10^{-1}$

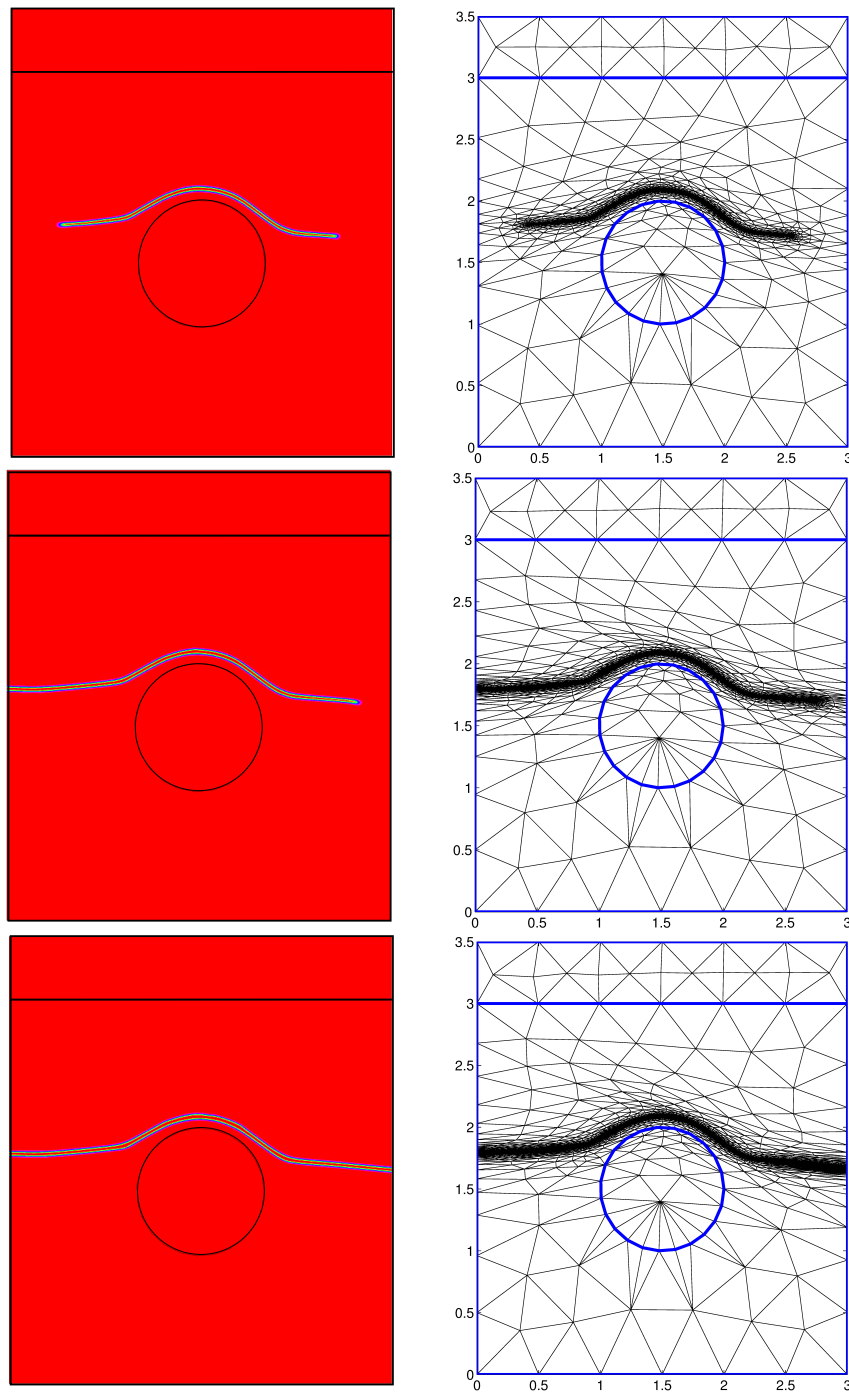


Figure 4: Traction of a fiber-reinforced matrix. Time evolution of the v_h -field (left): $t = 0.30$ (top), $t = 0.38$ (center), and $t = 0.40$ (bottom); corresponding adapted meshes (right) with $\varepsilon = 10^{-2}$

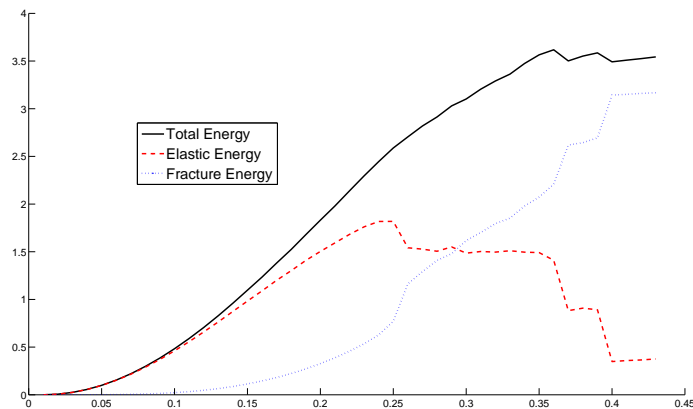


Figure 5: Traction of a fiber-reinforced matrix. Time evolution of the energy

Figure 5 shows the time evolution of the energy. The elastic energy (dashed line) is associated with the first term in the integral over Ω in (6), while the fictitious crack energy (dash-dotted line) represents the second term. The black line is the sum of these two contributions. Theoretically, we expect the elastic energy to disappear after the collapse of the domain. On the contrary, a residual energy remains, due to the regularization parameter η in the model. Moreover, three sudden increases of the crack energy occur: the first at time $t = 0.24$, when a finite-length crack appears on top of the fiber; the second at time $t = 0.37$, when the domain breaks on one side; and the last takes place when the domain breaks down, at $t = 0.39$. This behavior is qualitatively comparable with the ones in Fig. 4 in [16] and in Fig. 3 in [7]. This corroborates the fact that anisotropic meshes do not affect the crack dynamics.

4.2 Crack Branching

The domain for the second test case is the cracked rectangular elastic sample shown in Fig. 2, right. The initial crack is horizontal and parallel to the upper and lower sides of the sample, while a displacement field of increasing magnitude and fixed orientation, θ , to the x_1 -axis, is applied to the horizontal sides. The later crack evolution is monitored for several values of θ . The final time is set to $T = 0.2$, and the total number of uniform time steps is $F = 20$. The final time is chosen when the crack is about to turn towards the bottom right corner of the domain. The key issues of this problem is the correct prediction of the actual branching angle of the crack, in particular when the applied displacement field is not orthogonal to the domain border. For this purpose, we resort to a suitable mesh adaptation strategy.

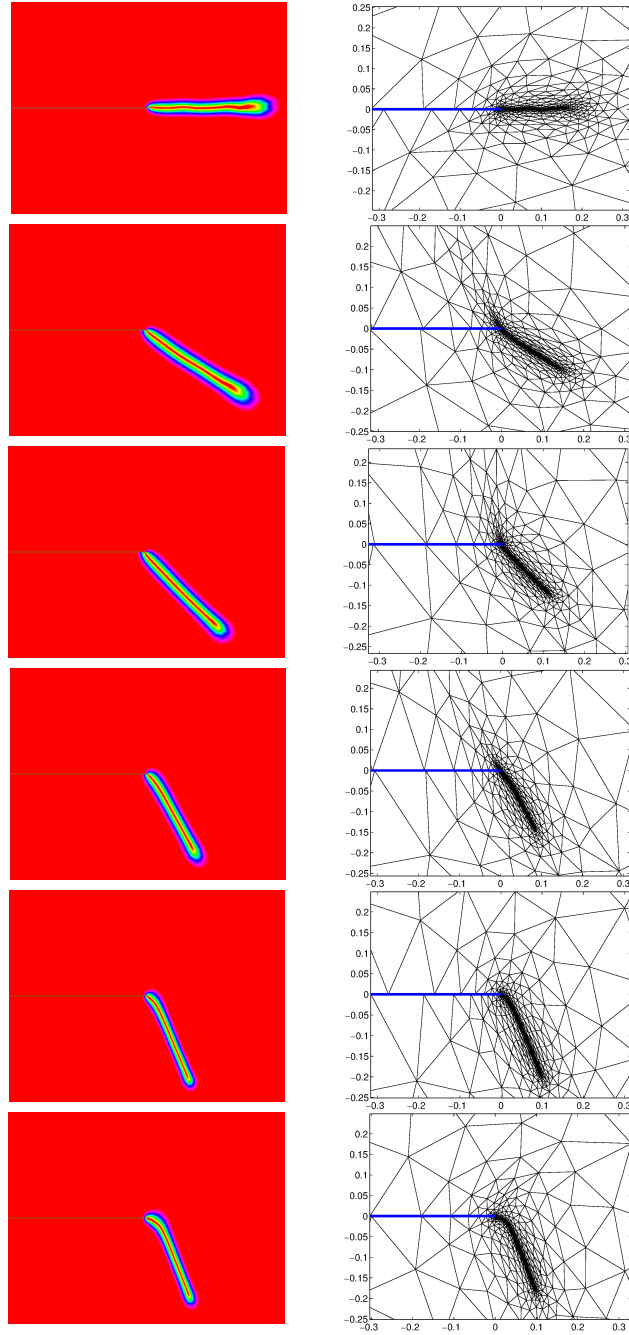


Figure 6: Crack branching. Distribution of the v_h -field around the tip of the initial crack (left) and final adapted mesh (right) for $\theta = \pi/2, \pi/4, \pi/6, \pi/20, \pi/60, 0$, top-down

In particular, we identify Ω with the square domain $(-1.5, 1.5)^2$, $\Omega_D = \Omega_D - \cup$

Ω_{D^+} with $\Omega_{D^-} = (-1.5, 1.5) \times (-1.5, -1.3)$ and $\Omega_{D^+} = (-1.5, 1.5) \times (1.3, 1.5)$, \mathbf{g}_D is

$$\mathbf{g}_D(t) = \begin{cases} (t \cos(\theta), t \sin(\theta)) & \text{on } \Omega_{D^+} \\ (-t \cos(\theta), -t \sin(\theta)) & \text{on } \Omega_{D^-} \end{cases} \quad (28)$$

and the model parameters are

$$\varepsilon = 10^{-2}, \quad \eta = 10^{-5}, \quad \gamma_A = \gamma_B = 10^{-5}, \quad \lambda = \frac{Yp}{(1+p)(1-2p)}, \quad \mu = \frac{Y}{2(1+p)},$$

with $Y = 45$ and $p = 0.18$. The tolerances of Algorithm 3.1 are

$$\text{VTOL} = 10^{-4}, \quad \text{CRTOL} = 3 \cdot 10^{-4}, \quad \text{REFTOL} = 10^{-3}, \quad \text{MESHTOL} = 10^{-2}.$$

Figure 6 gathers the v_h -field and the corresponding anisotropic adapted mesh at the final time, for several orientations θ . The cardinality of the meshes in Fig. 6 is 2941, 1268, 1652, 1302, 1570, 3804, in top-down order. Notice that the mesh adaptive procedure identifies the configurations associated with $\theta = \pi/2$ and $\theta = 0$ as being the most challenging. In all cases, the mesh closely matches the crack path, with a very thin thickness of the adapted area. The anisotropic features of the meshes are highlighted by the values of the maximum aspect ratio, which varies between 28, for $\theta = \pi/20$, and 384, for $\theta = 0$. Moreover, when $\theta = 0$, in contrast to [7], where it appears an unphysical symmetric crack branching, we obtain a crack which moves straight a very short distance, before turning downwards but with a slightly smaller angle than expected. In practice, we are able to predict reliably the crack branching for $\theta \gtrsim 3^\circ$. Figure 7 shows the branching angle as a function of the orientation θ . This angle has been computed by picking the angle at which the distribution of the unit vectors, $\mathbf{r}_{1,K}$, gathered in bins of 20 angles each, over the rectangle $[0, 0.08] \times [-0.08, 0]$ is a maximum. On comparing our results with the ones in [7], we observe a good agreement, with the additional capability of correctly simulating the physical behavior for $3^\circ \lesssim \theta \lesssim 7^\circ$, by enlarging the range of reliability of the numerical tool in [7] where $\theta \gtrsim 7^\circ$.

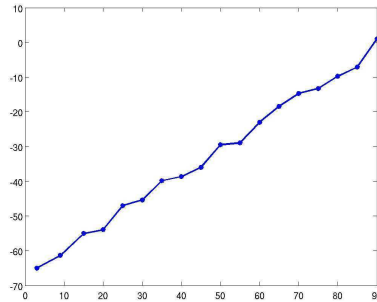


Figure 7: Crack branching. Branching angle as a function of the impressed displacement orientation

5 Conclusions

We have extended the anisotropic approach provided in [4] for the anti-plane case to the more challenging plane-strain framework. This implies moving from a scalar to a vector elastic problem. The proposed Algorithm 3.1 has been shown to correctly identifying the physical crack path, under reasonable choices of the physical and algorithmic parameters, aware also of the theoretical limits of the adopted mechanical model. In particular, in the crack branching test case, the proposed procedure allowed us to broaden the range of applicability of this model, with respect to what studied in [7]. Another interesting issue to be investigated is a proper tuning of the modeling parameters, such as ε , η , and also of the physical parameters λ and μ . In Sect. 4.1, we tackle to a some extent the sensitivity to ε by highlighting the actual influence of ε on the crack thickness. A more thorough investigation has been carried out in [3] in the anti-plane case. We have also introduced a generalized version of the algorithm proposed in [4]. In particular, Algorithm 3.1 employs the new parameter, namely `nMIN`, through which we can adjust in a more precise way the interplay between the minimization of the functional and the adaptation of the mesh. In future developments, we shall be concerned with the study of more general mathematical models, such as the ones introduced in [9], for a possible comparison with actual experimental tests.

References

- [1] Ambrosio, L., Tortorelli, V.M.: Approximation of functionals depending on jumps by elliptic functionals via γ -convergence. *Comm. Pure Appl. Math.* **43**(8), 999–1036 (1990)
- [2] Amestoy, M.: *Propagations de Fissures en Élasticité Plane*. Thèse d’Etat, Paris (1987)
- [3] Artina, M., Fornasier, M., Micheletti, S., Perotto, S.: Anisotropic adaptive meshes for brittle fractures: parameter sensitivity. In: A. Abdulle, S. Deparis, D. Kressner, F. Nobile (eds.) *Numerical Mathematics and Advanced Applications. Proceedings of ENUMATH 2013*, *Lect. Notes Comput. Sci. Eng.* Springer (2014). To appear
- [4] Artina, M., Fornasier, M., Micheletti, S., Perotto, S.: Anisotropic mesh adaptation for crack detection in brittle materials. *MOX Report 20/2014* (2014)
- [5] Artina, M., Fornasier, M., Solombrino, F.: Linearly constrained nonsmooth and nonconvex minimization. *SIAM J. Optim.* **23**(3), 1904–1937 (2013)

- [6] Border, M., Verhoosel, C., Scott, M., Hughes, T., Landis, C.: A phase-field description of dynamic brittle fracture. *Comput. Methods Appl. Mech. Engrg* **217-220**, 77–95 (2012)
- [7] Bourdin, B., Francfort, G., Marigo, J.J.: Numerical experiments in revisited brittle fracture. *J. Mech. Phys. Solids* **48**(4), 797–826 (2000)
- [8] Burke, S., Ortner, C., Süli, E.: An adaptive finite element approximation of a variational model of brittle fracture. *SIAM J. Numer. Anal* **48**(3), 980–1012 (2010)
- [9] Burke, S., Ortner, C., Süli, E.: An adaptive finite element approximation of a generalized Ambrosio-Tortorelli functional. *Math. Models Methods Appl. Sci.* **23**(9), 1663–1697 (2013)
- [10] Chambolle, A., Dal Maso, G.: Discrete approximation of the Mumford-Shah functional in dimension two. *M2AN Math. Model. Numer. Anal.* **33**(4), 651–672 (1999)
- [11] Ciarlet, P.G.: *The Finite Element Method for Elliptic Problems*. North-Holland, Amsterdam (1978)
- [12] Ciarlet, P.G., Raviart, P.A.: Maximum principle and uniform convergence for the finite element method. *Comput. Methods Appl. Mech. Engrg* **2**(1), 17–31 (1973)
- [13] Clément, P.: Approximation by finite element functions using local regularization. *RAIRO Anal. Numér.* **2**, 77–84 (1975)
- [14] Dal Maso, G.: *An Introduction to Γ -convergence*. Birkhäuser, Basel (1993)
- [15] Dedè, L., Micheletti, S., Perotto, S.: Anisotropic error control for environmental applications. *Appl. Numer. Math.* **58**(9), 1320–1339 (2008)
- [16] Del Piero, G., Lancioni, G., March, R.: A variational model for fracture mechanics: numerical experiments. *J. Mech. Phys. Solids* **55**, 2513–2537 (2007)
- [17] Formaggia, L., Perotto, S.: New anisotropic a priori error estimates. *Numer. Math.* **89**(4), 641–667 (2001)
- [18] Formaggia, L., Perotto, S.: Anisotropic error estimates for elliptic problems. *Numer. Math.* **94**, 67–92 (2003)
- [19] Francfort, G., Marigo, J.J.: Revisiting brittle fracture as an energy minimization problem. *J. Mech. Phys. Solids* **46**(8), 1319 – 1342 (1998)
- [20] George, P.L., Borouchaki, H.: *Delaunay Triangulation and Meshing. Application to Finite Elements*. Edition Hermès, Paris (1998)

- [21] Hecht, F.: New developments in Freefem++. *J. Numer. Math.* **20**(3-4), 251–265 (2012)
- [22] Korotov, S., Křížek, M., Neittaanmäki, P.: Weakened acute type condition for tetrahedral triangulations and the discrete maximum principle. *Math. Comp.* **70**(233), 107–119 (2001)
- [23] Lions J. L. and Magenes, E.: *Non-Homogeneous Boundary Value Problems and Applications*, vol. I. Springer-Verlag, Berlin (1972)
- [24] Micheletti, S., Perotto, S.: Reliability and efficiency of an anisotropic Zienkiewicz–Zhu error estimator. *Comput. Methods Appl. Mech. Engrg* **195**(9), 799–835 (2006)
- [25] Micheletti, S., Perotto, S.: Output functional control for nonlinear equations driven by anisotropic mesh adaption: the Navier-Stokes equations. *SIAM J. Sci. Comput.* **30**(6), 2817–2854 (2008)
- [26] Micheletti, S., Perotto, S.: The effect of anisotropic mesh adaptation on PDE-constrained optimal control problems. *SIAM J. Control. Optim.* **49**(4), 1793–1828 (2011)
- [27] Micheletti, S., Perotto, S., Picasso, M.: Stabilized finite elements on anisotropic meshes: a priori error estimates for the advection–diffusion and the Stokes problems. *SIAM J. Numer. Anal.* **41**(3), 1131–1162 (2003)
- [28] Miehe, C., Hofacker, M., Fabian, W.: A phase field model rate-independent crack propagation: Robust algorithmic implementation based on operator splits. *Comput. Methods Appl. Mech. Engrg* **199**(45-48), 2765–2778 (2010)
- [29] Strang, G., Fix, G.J.: *An Analysis of the Finite Element Method*, vol. 212. Prentice-Hall, Inc., Englewood Cliffs (1973)
- [30] Thomée, V.: *Galerkin Finite Element Methods for Parabolic Problems*, vol. 25. Springer-Verlag, Berlin (1997)

MOX Technical Reports, last issues

Dipartimento di Matematica “F. Brioschi”,
Politecnico di Milano, Via Bonardi 9 - 20133 Milano (Italy)

- 21/2014** ARTINA, M.; FORNASIER, M.; MICHELETTI, S.; PEROTTO, S.
The benefits of anisotropic mesh adaptation for brittle fractures under plane-strain conditions
- 20/2014** ARTINA, M.; FORNASIER, M.; MICHELETTI, S.; PEROTTO, S.
Anisotropic mesh adaptation for crack detection in brittle materials
- 19/2014** L.BONAVENTURA; R. FERRETTI
Semi-Lagrangian methods for parabolic problems in divergence form
- 18/2014** TUMOLO, G.; BONAVENTURA, L.
An accurate and efficient numerical framework for adaptive numerical weather prediction
- 17/2014** DISCACCIATI, M.; GERVASIO, P.; QUARTERONI, A.
Interface Control Domain Decomposition (ICDD) Method for Stokes-Darcy coupling
- 16/2014** DEDE, L.; JAGGLI, C.; QUARTERONI, A.
Isogeometric numerical dispersion analysis for elastic wave propagation
- 15/2014** ESFANDIAR, B.; PORTA, G.; PEROTTO, S.; GUADAGNINI, A;
Anisotropic mesh and time step adaptivity for solute transport modeling in porous media
- 14/2014** DASSI, F.; FORMAGGIA, L.; ZONCA, S.
Degenerate Tetrahedra Recovering
- 13/2014** BALLARIN, F.; MANZONI, A.; QUARTERONI, A.; ROZZA, G.
Supremizer stabilization of POD-Galerkin approximation of parametrized Navier-Stokes equations
- 12/2014** FUMAGALLI, I; PAROLINI, N.; VERANI, M.
Shape optimization for Stokes flow: a reference domain approach